TU Delft

Delft University of Technology

Document Version
Final published version

Licence
CC BY

Citation (APA)
Stone, E., Giani, S., Zappalá, D., & Crabtree, C. (2023). Convolutional neural network framework for wind turbine electromechanical fault detection. *Wind Energy*, *26*(10), 1082-1097. https://doi.org/10.1002/we.2857

Important note
To cite this publication, please use the final published version (if applicable).
Please check the document version above.

Copyright
In case the licence states “Dutch Copyright Act (Article 25fa)”, this publication was made available Green Open Access via the TU Delft Institutional Repository pursuant to Dutch Copyright Act (Article 25fa, the Taverne amendment). This provision does not affect copyright ownership.
Unless copyright is transferred by contract or statute, it remains with the copyright holder.

Sharing and reuse
Other than for strictly personal use, it is not permitted to download, forward or distribute the text or part of it, without the consent of the author(s) and/or copyright holder(s), unless the work is under an open content license such as Creative Commons.

Takedown policy
Please contact us and provide details if you believe this document breaches copyrights.
We will remove access to the work immediately and investigate your claim.

This work is downloaded from Delft University of Technology.

Check for updates

JGR Planets

RESEARCH ARTICLE
10.1029/2023JE007872

Special Section:
Solar System Science from JWST

An Energetic Eruption With Associated SO 1.707 Micron Emissions at Io's Kanehekili Fluctus and a Brightening Event at Loki Patera Observed by JWST

Imke de Pater[1,2], Emmanuel Lellouch[3], Darrell F. Strobel[4], Katherine de Kleer[5], Thierry Fouchet[3], Michael H. Wong[1], Bryan J. Holler[6], John Stansberry[6], Patrick M. Fry[7], Michael E. Brown[5], Dominique Bockelée-Morvan[3], Samantha K. Trumbo[8], L. N. Fletcher[9], Matthew M. Hedman[10], Edward M. Molter[2], Mark Showalter[11], Matthew S. Tiscareno[11], Stéphanie Cazaux[12], Ricardo Hueso[13], Statia Luszcz-Cook[14,15], Henrik Melin[9], Chris Moeckel[2], Alessandro Mura[16], Glenn Orton[17], Lorenz Roth[18,19], Joachim Saur[20], and Federico Tosi[16]

[1]Department of Astronomy, University of California, Berkeley, CA, USA, [2]Department of Earth & Planetary Science, University of California, Berkeley, CA, USA, [3]LESIA, Observatoire de Paris, Université PSL, Sorbonne Université, Université Paris Cité, CNRS, Meudon, France, [4]Departments of Earth & Planetary Sciences and Physics & Astronomy, Johns Hopkins University, Baltimore, MD, USA, [5]Division of Geological and Planetary Sciences, Caltech, Pasadena, CA, USA, [6]Space Telescope Science Institute, Baltimore, MD, USA, [7]University of Wisconsin, Madison, WI, USA, [8]Cornell Center for Astrophysics and Planetary Science, Cornell University, Ithaca, NY, USA, [9]School of Physics and Astronomy, University of Leicester, University Road, Leicester, UK, [10]Department of Physics, University of Idaho, Moscow, ID, USA, [11]SETI Institute, Mountain View, CA, USA, [12]Faculty of Aerospace Engineering Astrodynamics & Space Missions, Delft, The Netherlands, [13]Escuela de Ingeniería de Bilbao, Universidad del País Vasco, Bilbao, Spain, [14]Department of Astronomy, Columbia University, New York City, NY, USA, [15]Astrophysics Department, American Museum of Natural History, New York, NY, USA, [16]Istituto Nazionale di AstroFisica—Istituto di Astrofisica e Planetologia Spaziali (INAF-IAPS), Rome, Italy, [17]Jet Propulsion Lab, California Institute of Technology, Pasadena, CA, USA, [18]Space and Plasma Physics, KTH Royal Institute of Technology, Stockholm, Sweden, [19]European Southern Observatory, Garching bei München, Germany, [20]Institute of Geophysics and Meteorology, University of Cologne, Koeln, Germany

Abstract We observed Io with the James Webb Space Telescope (JWST) while the satellite was in eclipse, and detected thermal emission from several volcanoes. The data were taken as part of our JWST-ERS program #1373 on 15 November 2022. Kanehekili Fluctus was exceptionally bright, and Loki Patera had most likely entered a new brightening phase. Spectra were taken with NIRSpec/IFU at a resolving power $R \approx 2{,}700$ between 1.65 and 5.3 μm. The spectra were matched by a combination of blackbody curves that showed that the highest temperature, ~1,200 K, for Kanehekili Fluctus originated from an area ~0.25 km^2 in size, and for Loki Patera this high temperature was confined to an area of ~0.06 km^2. Lower temperatures, down to 300 K, cover areas of ~2,000 km^2 for Kanehekili Fluctus, and ~5,000 km^2 for Loki Patera. We further detected the $a^1\Delta \Rightarrow X^3\Sigma^-$ 1.707 μm rovibronic forbidden SO emission band complex over the southern hemisphere, which peaked at the location of Kanehekili Fluctus. This is the first time this emission has been seen above an active volcano, and suggests that the origin of such emissions is ejection of SO molecules directly from the vent in an excited state, after having been equilibrated at temperatures of ~1,500 K below the surface, as was previously hypothesized.

Plain Language Summary We observed Io with JWST in November 2022 while the satellite was in Jupiter's shadow, and glowing volcanoes show up without being (partially) obscured by reflected sunlight. We detected the volcanoes Loki Patera and Kanehekili Fluctus; the latter was exceptionally bright, and Loki Patera had likely entered a new brightening phase. Both volcanoes show erupting lavas at temperatures of at least 1,200 K, originating at a vent of ~0.25 km^2 in size for Kanehekili Fluctus and <0.1 km^2 for Loki Patera. In addition to lava, Kanehekili Fluctus spews out gases, and we detected, for the first time, SO emission at 1.707 μm right over the volcano. This is the first time this emission has been seen above an active volcano, and suggests that such emissions are produced by SO molecules immediately upon leaving the vent.

Key Points:

- James Webb Space Telescope observations detected an energetic eruption at Kanehekili Fluctus, and a new brightening event at Loki Patera
- The erupting lavas have a temperature of at least 1,200 K over an area of ~0.25 km^2 or less
- We detected, for the first time, a clear association of the 1.707 micron forbidden SO emissions with an active volcano

Correspondence to:
I. de Pater,
imke@berkeley.edu

Citation:
de Pater, I., Lellouch, E., Strobel, D. F., de Kleer, K., Fouchet, T., Wong, M. H., et al. (2023). An energetic eruption with associated SO 1.707 micron emissions at Io's Kanehekili Fluctus and a brightening event at Loki Patera observed by JWST. *Journal of Geophysical Research: Planets*, *128*, e2023JE007872. https://doi.org/10.1029/2023JE007872

Received 25 APR 2023
Accepted 12 JUL 2023

Author Contributions:
Conceptualization: Imke de Pater, Emmanuel Lellouch
Data curation: Imke de Pater, Emmanuel Lellouch, Thierry Fouchet, Michael H. Wong
Investigation: Imke de Pater
Methodology: Imke de Pater, Bryan J. Holler, John Stansberry, Matthew M. Hedman, Mark Showalter
Software: Imke de Pater, Bryan J. Holler, John Stansberry, Patrick M. Fry, Michael E. Brown

© 2023. The Authors.
This is an open access article under the terms of the Creative Commons Attribution-NonCommercial-NoDerivs License, which permits use and distribution in any medium, provided the original work is properly cited, the use is non-commercial and no modifications or adaptations are made.

1. Introduction

Jupiter's satellite Io is the most volcanically active body in our Solar System. Its extreme volcanism is caused by strong tidal heating induced by an orbital eccentricity that is forced by Jupiter and the 4:2:1 Laplace orbital

Visualization: Imke de Pater, Chris Moeckel
Writing – original draft: Imke de Pater, Darrell F. Strobel
Writing – review & editing: Imke de Pater, Emmanuel Lellouch, Darrell F. Strobel, Katherine de Kleer, Thierry Fouchet, Michael H. Wong, Bryan J. Holler, John Stansberry, Patrick M. Fry, Michael E. Brown, Dominique Bockelée-Morvan, Samantha K. Trumbo, L. N. Fletcher, Matthew M. Hedman, Edward M. Molter, Mark Showalter, Matthew S. Tiscareno, Stéphanie Cazaux, Ricardo Hueso, Statia Luszcz-Cook, Henrik Melin, Chris Moeckel, Alessandro Mura, Glenn Orton, Lorenz Roth, Joachim Saur, Federico Tosi

resonance between Io, Europa, and Ganymede (Peale et al., 1979). The composition and temperature of Io's magma, however, which are indicative of the state of Io's highly processed mantle, are poorly constrained. Blackbody radiation from volcanic hot spots is observable in the near and mid-infrared, but reflected sunlight from Io's bright surface overwhelms the thermal emission at wavelengths shortwards of ∼3 μm (de Pater et al., 2004, 2017). The shorter wavelengths are most sensitive to high-temperature eruptions (1,000–2,000 K blackbody curves peak at 3 and 1.5 μm, resp.), which are most intriguing because temperatures over ∼1,800 K are indicative of magnesium-rich ultra-mafic magma compositions (Davies, 2007); such eruptions do not now happen on Earth, but were suggested to be widespread on early Earth, and hence may provide an analogue for Earth's formative years (Williams et al., 2000). Volcanic thermal emissions at such short wavelengths over small regions can only be detected when Io is in Jupiter's shadow, so they are not obscured by reflected sunlight. During an eruption, rapidly cooling lava flowing away from the eruption site leads to temperatures that vary from the highest (eruption) component down to essentially the equilibrium temperature of the satellite. Such a temperature "field" can be characterized by measuring the hot spot's emission over a broad wavelength range, preferably from $\lesssim$1 μm up to ∼20 μm.

Spectra of Io in eclipse may reveal plume emissions, such as the (forbidden) $a^1\Delta \Rightarrow X^3\Sigma^-$ rovibronic SO emission complex at 1.707 μm. This emission band complex was first detected in 1999 in spectra integrated over Io's disk (de Pater et al., 2002). The authors proposed that the emissions were produced by SO molecules that were excited into the (meta-stable) $a^1\Delta$ state at a thermodynamic quenching temperature of ∼1,500 K (i.e., they were in Local Thermodynamic Equilibrium, LTE, at ∼1,500 K); they would radiate upon exiting the volcanic vent, and not be excited again. Since at the time Loki Patera was in a brightening phase (Howell et al., 2001), the authors suggested Loki Patera as the source of the emissions. More recent, spatially resolved observations of this forbidden SO emission may suggest a more complex origin: (a) there is no clear connection between the SO spatial distribution and the location of hot spots (de Pater et al., 2007, 2020), and (b) some parts of the emission band, in particular near 1.69 and 1.717 μm, are highly suggestive of non-LTE effects (i.e., gas that did not get thermodynamically equilibrated at ∼1,500 K) (Bernath & Bittner, 2020; de Kleer, de Pater, & Ádámkovics, 2019; de Pater et al., 2002; de Pater et al., 2020).

High-spatial-resolution observations of Io in eclipse, such as those needed to trace and characterize Io's eruptions, are difficult to conduct from the ground. Previous disk-resolved ground-based observations were conducted using the Keck telescope equipped with adaptive optics (AO) to correct for blurring through Earth's atmosphere. This requires the presence of an uneclipsed Galilean satellite within 30″ of Io for wavefront sensing. To build up enough signal-to-noise on the SO emission complex, one needs to observe Io during an eclipse that lasts for an hour or more. This can only be achieved at large ($\gtrsim$10°) solar phase angles, and the Galilean satellite used for AO wavefront sensing must be available for the entire hour. Such occasions are quite rare, and have been performed only three times since the first detection of SO (de Pater et al., 2007, 2020).

The James Webb Space Telescope (JWST) presents an opportunity to observe Io's 1.707-μm forbidden SO emission without the need for AO. We proposed to observe Io in eclipse with JWST as part of our Early Release Science Program (ERS #1373). The challenging observations of Io in eclipse next to Jupiter's very bright disk presented a valuable opportunity to explore JWST's capabilities for Solar System science, in close alignment with the primary goal of this ERS program (de Pater et al., 2022). In this paper, we present results on spectra of the two brightest hot spots detected on Io, Kanehekili Fluctus and Loki Patera, and on the spatial distribution of the 1.707-μm SO emissions, that is, the SO population in the excited $a^1\Delta$ state.

2. JWST Observations

2.1. Observations and Data Reduction

Io was observed on UT 15 November 2022 with the integral field unit (IFU) of JWST's near-infrared spectrograph NIRSpec. As planned, Io was in eclipse. Spectra were obtained in two settings: (a) G395H/F290LP with a total exposure time of 257 s, and (b) G235H/F170LP with a total exposure time of 515 s. Together these grisms cover a wavelength range of 1.65–5.3 μm at a resolving power $R \sim 2{,}700$. Figure 1 shows the geometry of the Io-Jupiter system during our observations. Observations focused on the SO emission complex were also conducted (in G140H/F100LP—intended to cover 0.97–1.89 μm at $R \sim 1{,}000$, at an exposure time of 2800 s), but Io was behind

21699100, 2023, 8, Downloaded from https://agupubs.onlinelibrary.wiley.com/doi/10.1029/2023JE007872 by Technical University Delft, Wiley Online Library on [15/08/2023]. See the Terms and Conditions (https://onlinelibrary.wiley.com/terms-and-conditions) on Wiley Online Library for rules of use; OA articles are governed by the applicable Creative Commons License

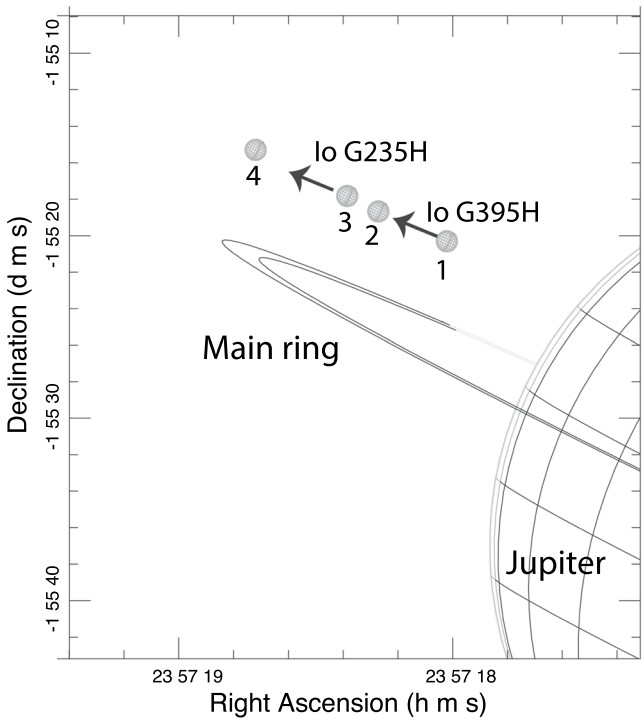

Figure 1. Geometry of Io in eclipse observations as seen from the James Webb Space Telescope. After Io has emerged from being occulted by Jupiter, we observed with the G395H grism while Io moved from point 1 to 2; and in the G235H grism while it moved from point 3 to 4. Figure is adapted from the Planetary Ring Node; http://pds-rings.seti.org/tools/.

Jupiter at the time, and hence no data were obtained; the observations are planned for a repeat in August 2023. A summary of the successful observations is provided in Table 1.

The IFU field of view is 3″ × 3″, with a pixel size of 0.1″. We therefore obtained almost 12 pixels across Io's 1.171″ disk. The Central Meridian Longitude ranged over 13–15°W for the G395H data, and 15–18.5°W for G235H. The sub-observer latitude was 2.36°. JWST uses an up-the-ramp readout mode, where the array is read out non-destructively at intervals defined by the readout pattern. We used the readout pattern NRSRAPID, which saves every frame as a group (some other patterns combine several frames into a group). We used 2 groups per integration. Each integration begins with a detector reset. The G395H data had 2 integrations for each of the 4 dithers; the G235H data had 4 integrations for each of the 4 dithers. Photons are accumulated continuously during an integration. However, users may delete groups from an integration when starting from the uncalibrated raw data (uncal) to reduce issues with detector saturation. As discussed below, we utilized both 1-group data cubes (removing the second group) and 2-group data cubes in our analysis. For more information, see https://jwst-docs.stsci.edu/understanding-exposure-times.

The Observatory Scheduling Software used was version 8.4.14. The raw (uncal) data were calibrated with the experimental pipeline version 1.8.3.dev69+g67b11ff5, and CRDS (Calibration References Data System) files CRDS_VER = 11.16.16 & CRDS_CTX = jwst_1023.pmap. Two consecutive pipelines are run: Detector1Pipeline produces the level 1 data ("rate" and "rateints" files), and Spec2Pipeline produces the level 2 data ("cal" and final images per dither). We followed the procedure described by Trumbo et al. (2023) to correct the data for the frequency-dependent 1/f noise in the gratings. To characterize this noise, we started with the Level 1 rate files, and used the Level 2 cal files to determine which pixels in the rate files to use to make an image of the 1/f noise. The cal files show which pixels are illuminated, and hence these pixels should not be used to determine the 1/f noise image. For each unilluminated pixel in the rate image, we took the median of all pixels in a column within ±150 rows, which resulted in an image that clearly showed the 1/f modulation. We tested how many pixels to use in the median by running the procedure twice more, first taking the median along the entire column, and second taking the median over ±250 pixels; as in Trumbo et al. (2023), using ±150 pixels gave the best results. We subtracted this 1/f noise image from the rate file, and reran the standard Level 2 pipeline on these new rate files to obtain the final calibrated images for each dither. We used the coordinate system "ifualign" in the CubeBuild model. We experimented with different weighting options in the cube_build. weighting function, and found no noticeable difference compared to the standard weighting option.

Since several of the brightest pixels in the G395H grism (on Kanehekili Fluctus) were saturated, we repeated the process above by using just the first of the two groups in the integration. Since the flux calibration is based on the up-the-ramp slope, we determined a wavelength-dependent calibration factor for the 1-group image data cubes by comparing the intensity of these data cubes on our second brightest spaxels (Loki Patera, which were not saturated) to the 2-group flux densities in these spaxels. Based on this comparison we scaled the wavelength-dependent intensity of the 1-group data cubes up by ∼10%.

Table 1
James Webb Space Telescope Observations of Io-in-Eclipse, 15 November 2022

UT time hr:m:s–hr:m:s	Disperser/Filter	Wavelength μm	Δ[a] AU	Longitude[b] °	Latitude[b] °
08:37:01–08:50:28	G395H/F290LP	2.87–5.27	4.308	13–15	2.36
08:55:37–09:13:22	G235H/F170LP	1.66–3.17	4.308	15–18.5	2.36

[a]Sub-observer (JWST) distance. [b]Sub-observer (JWST) W. longitude and latitude.

21699100, 2023, 8, Downloaded from https://agupubs.onlinelibrary.wiley.com/doi/10.1029/2023JE007872 by Technical University Delft, Wiley Online Library on [15/08/2023]. See the Terms and Conditions (https://onlinelibrary.wiley.com/terms-and-conditions) on Wiley Online Library for rules of use; OA articles are governed by the applicable Creative Commons License

21699100, 2023, 8, Downloaded from https://agupubs.onlinelibrary.wiley.com/doi/10.1029/2023JE007872 by Technical University Delft, Wiley Online Library on [15/08/2023]. See the Terms and Conditions (https://onlinelibrary.wiley.com/terms-and-conditions) on Wiley Online Library for rules of use; OA articles are governed by the applicable Creative Commons License

The calibration procedure generates calibrated image data cubes in units of MJy/sr. We then align each set of four dithers using a Fast Fourier transform (FFT) cross-correlation algorithm in IDL. We then median averaged the data cubes which helped to remove many cosmic ray hits and bad pixels. This resulted in four image data cubes, each covering a different wavelength range: G235H, with the detector NRS1 covering the wavelength range 1.65–2.37 μm; G235H, with the detector NRS2 covering 2.42–3.17 μm; G395H, NRS1: 2.86–3.99 μm; G395H, NRS2: 4.08–5.27 μm. We determined the wavelength-dependent background emission in areas around Io, and subtracted this from the image data cubes; this removed broad emission features at 1.86–1.92 μm (shown in Figure 7a in Section 3.2) and at 2.6–2.8 μm. These features correspond to peaks in Jupiter's brightness (Rayner et al., 2009), and so most likely are due to stray light from the planet. To further clean up the image data cubes, we inspected each image and replaced remaining cosmic ray hits and other bad pixels with values at the same pixel location but 1 or 2 spectral channels away in the image data cube. No pixels on Io at or near the 1.707 μm SO emission band were affected. Since the pixel scale is relatively coarse (0.1″), the pixel-to-pixel variation is too large to replace bad pixels with the median of surrounding points.

2.2. Units

The NIRSpec calibration software produces calibrated spectral radiance cubes, L_ν, in MJy/sr. We converted the data into other units for easier comparison with previous data. We converted our image data cubes into photon spectral radiance, L_q, in photons/s/cm^2/μm/sr via

$$L_q = L_\nu \; S_{MJy} \; \frac{\lambda}{hc} \; \frac{c}{\lambda^2} = L_\nu \times \left(1.51 \times 10^9/\lambda\right), \tag{1}$$

where $S_{MJy} = 10^{-17}$ erg/s/cm^2/Hz, hc/λ is the photon energy, $h = 6.63 \times 10^{-27}$ erg s, and c/λ^2 converts from power per unit frequency to power per unit wavelength, with wavelength λ in μm. We also constructed a second data cube F_λ in erg/s/cm^2/μm via

$$F_\lambda = L_\nu \; S_{MJy} \; \frac{c}{\lambda^2} \times p_{sr} = L_\nu \times \left(3.0 \times 10^{-3} \times p_{sr}/\lambda^2\right), \tag{2}$$

where $c = 3.00 \times 10^{14}$ μm/s (same length unit as wavelength), and $p_{sr} = 2.35 \times 10^{-13}$, the area of a 0.1″ pixel in steradians.

The latter units were then easily converted into a distance-independent radiant flux, GW/μm/sr, by further multiplying the images by $\Delta^2 \times 10^{-3}/10^9$, where Δ is Io's distance from JWST in m. To obtain the distance-independent flux for spectra in photons/s/cm^2/μm/sr, we similarly convert the units to photons/s/μm/sr by multiplying the image data cubes by $\Delta^2 \times p_{sr} \times 10^4$. The radiance in GW/$\mu$m or photons/s/$\mu$m can be obtained by multiplying the numbers by a factor of π (Davies, 2022).

3. Results

3.1. Images and Spectra of Io's Hot Spots

Images of Io in eclipse at 1.66, 3.0, and 5.0 μm extracted from the image data cubes are shown in Figures 2a–2c. We distinguish two bright regions on these images, which have been identified as Loki Patera and Kanehekili Fluctus, as discussed below. A reprojection of the 1.66-μm image, superposed on a USGS map of Io, is shown in Figure 3a. Since Io was in eclipse, we cannot determine the limb of the satellite. We also cannot use the NIRSpec pointing itself, since the observations combine a 0.1″ (1-σ) pointing uncertainty dominated by guide star catalog errors, with a 0.2″ systematic NIRSpec IFU pointing offset. In practice we noticed that the position of Io was off by ∼0.5″ compared to the NIRSpec pointing. We instead assumed the bright source on the East limb to be Loki Patera, since infrared emission from this volcano is visible on every image of Io that targets the appropriate hemisphere. We adopted the center of Loki Patera to be at 308°W, 12°N (de Pater et al., 2017), and moved the "center" of Io on the original image until Loki Patera fell on the right longitude/latitude on the reprojected map. To determine the location of Loki Patera and the center of Io with subpixel precision, we increased the size of the image by a factor of 5, to get an effective pixel size of 0.02″ (i.e., we interpolated between pixels). Once we knew the center of the disk, we could determine the location of Io's limb in Figure 2, and identify the bright volcano as Kanehekili Fluctus. Several additional volcanoes also show some, though much fainter, continuum emission.

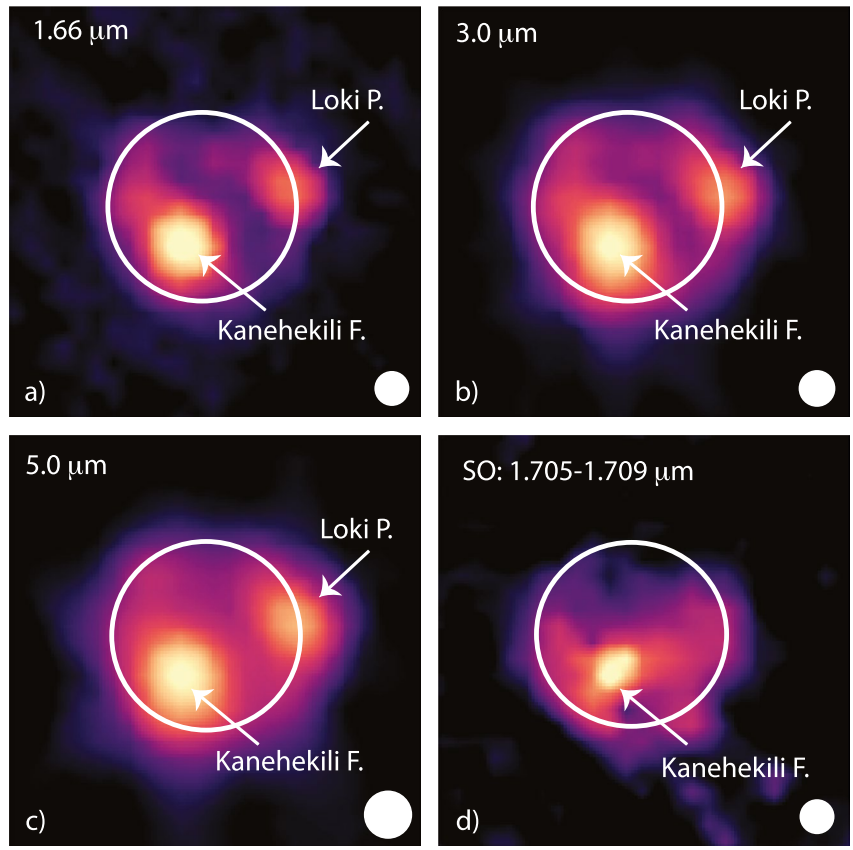

Figure 2. (a–c) James Webb Space Telescope images of Io in eclipse at 1.66, 3.0, and 5.0 μm. Each image is median-averaged over 20 channels, or 0.008 μm at 1.66 and 3.0 μm, and 0.013 μm at 5.0 μm. (d) An image of Io's SO emission, integrated over the center of the emission band (1.705–1.709 μm). The intensity scale on each panel is chosen such as to show the full range of emissions, using the Asinh scaling function and magma color scale in IDL's ATV. The circle shows the approximate limb of Io. Io's North pole is pointed up in each panel. The size of the point spread function, measured as the full width at half power from images of the star P330-E, is indicated in the lower right corner.

Spectra of the total intensity of Io, as well as the intensity of Loki Patera and Kanehekili Fluctus, are shown in Figure 4. The total intensity of each of the two volcanoes was determined by integrating the intensity in a circular aperture with a radius of 1 pixel, using the apphot.pro program in IDL (https://www.stsci.edu/~mperrin/software/sources/apphot.pro), after increasing the size of each image frame in the data cube by a factor of 5 to create sub-spaxels at a 0.02″-sized grid. We choose to look at aperture-summed spectra instead of single-pixel spectra in order to suppress the wiggles in individual spaxel spectra due to an undersampling of the point spread function (PSF) (examples of wiggles are still visible in the G395H spectra in the bottom row of Figure 6). The intensity of the volcanoes was corrected for the loss of flux due to the extent of the PSF by measuring the intensity of the star P330-E (Bohlin & Landolt, 2015) taken with the same grisms and the same small circular aperture in JWST program #01538. The ratio of this intensity to the total intensity of the star was ∼40% at the shortest wavelengths, down to ∼25% at the longest wavelengths. The measured intensity of Loki Patera and Kanehekili Fluctus was corrected for this wavelength-dependent loss of flux.

To facilitate comparison of these JWST spectra with previous measurements of Io in eclipse, we superposed the total flux densities of Io as measured on 24 September 1999 and 11 May 2008 (de Pater et al., 2017) on Figure 4. On 24 September 1999 Loki Patera was erupting, and had reached roughly 50% of its peak flux density during this brightening event; about 3 weeks later it was at its peak (Howell et al., 2001). In 2022, on August 15, 16, September 07 and 12, images of Io were obtained with the Near-infrared Camera NIRC2, coupled to the AO system on the Keck 2 telescope. The Keck images were reduced and the flux densities of these volcanoes were determined in the same manner as those published by, for example, (de Kleer & de Pater, 2016; de Pater et al., 2014). Those images captured the two volcanoes Loki Patera and Kanehili Fluctus (as well as several others), as shown in Figure 5, and summarized in Table 2.

21699100, 2023, 8, Downloaded from https://agupubs.onlinelibrary.wiley.com/doi/10.1029/2023JE007872 by Technical University Delft, Wiley Online Library on [15/08/2023]. See the Terms and Conditions (https://onlinelibrary.wiley.com/terms-and-conditions) on Wiley Online Library for rules of use; OA articles are governed by the applicable Creative Commons License

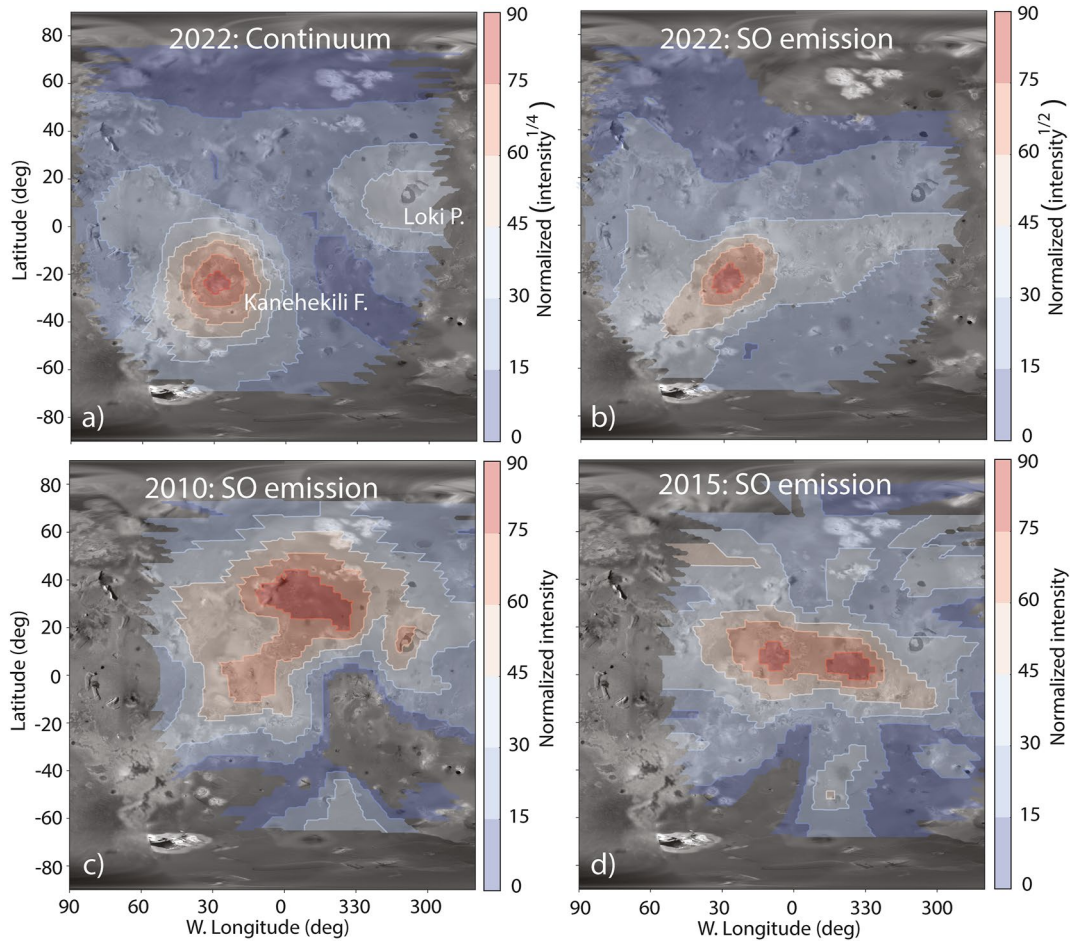

Figure 3. (a) A James Webb Space Telescope (JWST) map of Io's 1.66-μm emission. The intensity$^{1/4}$, normalized to 100 (i.e., the maximum intensity$^{1/4}$ is set equal to 100), is superposed on a USGS map of the satellite (https://astrogeology.usgs.gov/maps/io-voyager-galileo-global-mosaics). By using the intensity$^{1/4}$ we can also see emissions much fainter than Kanehekili Fluctus. (b) A JWST map of Io's SO emission from the JWST data, integrated over the center of the band (1.705–1.709 μm). The intensity$^{1/2}$, normalized to 100 (i.e., the maximum intensity$^{1/2}$ is set equal to 100), is superposed on the above USGS map of the satellite. We used the square root of the image here to also show fainter structures in the maps. The maximum intensity is 6.5×10^{27} photons/s/μm/sr (i.e., this value does not depend on the observer–Io distance; see Section 2.2). (c) A map of Io's SO emission as obtained from Keck data in 2010, integrated over the center of the emission band (1.705–1.709 μm). The scale is linear, normalized to 100, and the maximum intensity is 4.0×10^{27} photons/s/μm/sr (from de Pater et al. (2020)). (d) A map of Io's SO emission as obtained from Keck data in 2015, integrated over the center of the emission band (1.705–1.709 μm). The scale is linear, normalized to 100, and the maximum intensity is 1.1×10^{27} photons/s/μm/sr (from de Pater et al. (2020)).

On August 16 and September 12 Loki Patera was detected with an intensity of ∼12–15 GW/μm/sr at 4.67 μm and ∼2.5–3 GW/μm/sr at 3.67 μm. These intensities were corrected for the emission angle (ϵ) effect (i.e., correcting for the foreshortening effect of a surface area near the limb) by dividing the observed values by cos(ϵ). On both dates, Loki Patera is fainter than the JWST measurements, which were obtained ∼2 months later. Note, also, that we did not correct the JWST data for the emission angle effect in this graph to better show the observed spectra relative to Io's total intensity. In addition, so close to the limb, topography may affect the observed intensity, though likely would result in too low rather than too high values (de Kleer & de Pater, 2017). A correction for the emission angle would increase Loki Patera's intensity over its entire spectrum by a factor of 2.6, bringing it almost up to Kanehekili Fluctus' spectrum. (The emission angle effect for Kanehekili Fluctus would increase its intensity by ∼10%). Kanehekili Fluctus was imaged with the Keck telescope on August 15 and September 07, and is on the West limb on September 12. The Keck values for this volcano are also much fainter than what was measured by JWST. This compilation of data demonstrates that JWST captured Io during an extremely active period:

21699100, 2023, 8, Downloaded from https://agupubs.onlinelibrary.wiley.com/doi/10.1029/2023JE007872 by Technical University Delft, Wiley Online Library on [15/08/2023]. See the Terms and Conditions (https://onlinelibrary.wiley.com/terms-and-conditions) on Wiley Online Library for rules of use; OA articles are governed by the applicable Creative Commons License

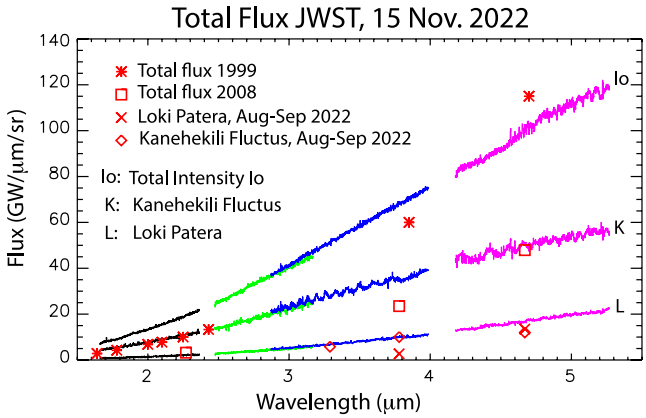

Figure 4. Spectra of the total intensity of the satellite Io, Loki Patera and Kanehekili Fluctus. The different colors of the spectra refer to the four different spectral regions of the G235H and G395H gratings. Superposed are the total flux densities of a few previous observations when Io was in eclipse, in 1999 and 2008, as indicated. Average intensities as measured for Loki Patera and Kanehekili Fluctus in August–September 2022, taken 2–3 months before the James Webb Space Telescope (JWST) observations, are also indicated; the latter values were corrected for the emission angle effect (see text and Table 2). If the JWST spectra for Loki Patera would be corrected for the emission angle effect it would be raised by a factor of 2.6, and be almost as bright as Kanehekili Fluctus.

Kanehekili Fluctus appears to be erupting, and Loki Patera appears to have entered a new brightening phase, as discussed in more detail in Section 4.

3.2. Forbidden SO Emission

When zooming in on the shortest wavelengths of the spectrum in Figure 4, one can distinguish the $a^1\Delta \Rightarrow X^3\Sigma^-$ rovibronic SO emission band centered at 1.707 μm, as shown in Figure 7. Panel (a) shows the intensity integrated over the disk over the 1.6–2.2 μm range, both before and after subtracting the wavelength-dependent background emission. Io's (hot spot) continuum emission was subsequently subtracted by fitting each spaxel in the image data cube by a second order polynomial, and subtracting this polynomial from each spaxel in the image data cube. The SO spectrum after subtraction of the continuum is shown in panel b of Figure 7. We show both the total SO emission, and the SO emission from Kanehekili Fluctus. Although we are confident that this technique provides the best wavelength-dependent image data cube of just the thermal emission, we caution the reader that the SO emission band complex is only a small ($\lesssim$ 10%–15%) fraction of the total flux, and indistinguishable from the noise in the continuum flux in a single spaxel. Despite this cautionary note, we note that the overall spectrum resembles previous spectra quite well, including the ∼1.71–1.72 μm wing and overall elevated emission at ∼1.685–1.705 μm. Note, though, that the latter is very close to the edge of the spectral band.

4. Discussion

4.1. Hot Spot Emissions

At 1.72 μm the peak total intensity from Io is $\sim 7 \times 10^{13}$ photons/s/cm^2/μm/sr, or 17 photons/s/cm^2/μm, which, after correcting for the observer–Io distance, is roughly twice as much as in 1999, 2002, and 2015, and 4 times more than in 2010 (de Pater et al., 2002, 2007, 2020). The increase in intensity as observed by JWST is also illustrated in Figure 4, which shows, in addition to the spectrum of Io's total flux density, the spectra of each

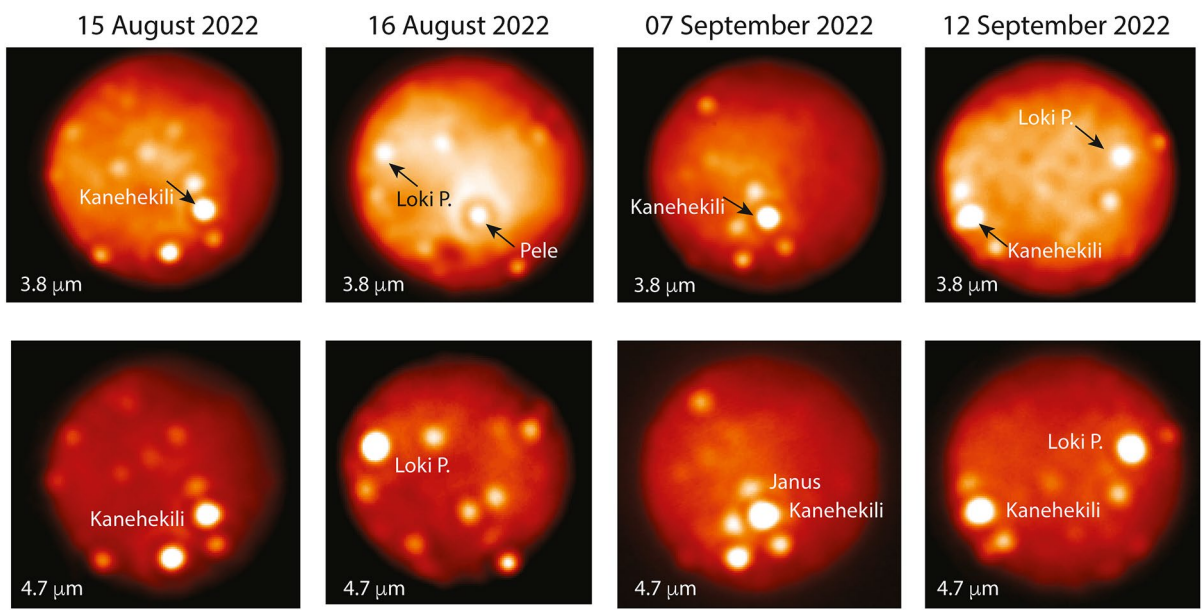

Figure 5. Images of Io taken with NIRC2 on the Keck 2 telescope about 2–3 months before the James Webb Space Telescope observations. The dates are listed at the top of the figure. The upper row shows images taken in L' (3.78 μm) band, the bottom row in Ms (4.67 μm) band, within about 2–3 min of each other.

21699100, 2023, 8, Downloaded from https://agupubs.onlinelibrary.wiley.com/doi/10.1029/2023JE007872 by Technical University Delft, Wiley Online Library on [15/08/2023]. See the Terms and Conditions (https://onlinelibrary.wiley.com/terms-and-conditions) on Wiley Online Library for rules of use; OA articles are governed by the applicable Creative Commons License

21699100, 2023, 8, Downloaded from https://agupubs.onlinelibrary.wiley.com/doi/10.1029/2023JE007872 by Technical University Delft, Wiley Online Library on [15/08/2023]. See the Terms and Conditions (https://onlinelibrary.wiley.com/terms-and-conditions) on Wiley Online Library for rules of use; OA articles are governed by the applicable Creative Commons License

Table 2
Keck Observations of Io in 2022

UT time month/day hr:m	Filter[a]	Wavelength μm	Δ[b] AU	Longitude[c] °	Latitude[c] °	Volcano	Intensity[d] GW/μm/sr
08/15 14:26	L'	3.78	4.20	52.4	2.71	Kanehekili F.	9.5 ± 1.0
08/15 14:30	Ms	4.67	4.20	52.9	2.71	Kanehekili F.	12.5 ± 1.3
08/15 14:36	PAH	4.67	4.20	53.8	2.71	Kanehekili F.	5.4 ± 0.7
08/16 14:54	L'	3.78	4.18	260.0	2.71	Loki P.	2.4 ± 0.3
08/16 14:57	Ms	4.67	4.18	260.4	2.71	Loki P.	12.4 ± 1.3
09/07 11:47	L'	3.78	4.01	32.4	2.72	Kanehekili F.	11 ± 3
09/07 11.50	Ms	4.67	4.01	32.8	2.72	Kanehekili F.	9 ± 3
09/07 11:53	PAH	3.29	4.01	33.3	2.72	Kanehekili F.	6.5 ± 1.5
09/12 13:09	L'	3.78	3.98	342.1	2.71	Kanehekili F.	10 ± 1
09/12 13:13	Ms	4.67	3.98	342.7	2.71	Kanehekili F.	14.5 ± 1.5
09/12 13:16	PAH	3.29	3.98	343.1	2.71	Kanehekili F.	5.5 ± 0.7
09/12 13:09	L'	3.78	3.98	342.1	2.71	Loki P.	3.0 ± 0.4
09/12 13:13	Ms	4.67	3.98	342.7	2.71	Loki P.	14.5 ± 1.5

[a]L' band spans 3.426–4.126 μm; Ms band spans the range 4.549–4.790 μm. [b]Geocentric distance. [c]Sub-observer W. longitude and latitude. [d]Total intensity of volcano, corrected for the emission angle effect.

Kanehekili Fluctus and Loki Patera. Clearly, Kanehekili Fluctus was extremely active during the JWST observations, much more so than 2–3 months earlier, in August-September, when observed with Keck (Figure 5, Table 2). Kanehekili Fluctus was also not particularly active in December 2018, in observations made by Juno during an eclipse (Mura et al., 2020). Even though the hot spot at that time was very close to the limb, the total power after correction for the emission angle effect did not exceed 10 GW/μm/sr at 4.78 μm at the time of that observation. Its intensity did also not peak above a few GW/μm/sr from 2014 to 2018 (de Kleer, de Pater, Molter, et al., 2019), nor have outbursts at Kanehekili Fluctus been seen in the Keck twilight zone program (https://www2.keck.hawaii.edu/inst/tda/TwilightZone.html#). Observations of Kanehekili Fluctus before 2014, however, have shown that it is highly variable over time (Cantrall et al., 2018; Davies et al., 2012). It is often invisible in the near-IR for many years. But when it is active, the intensity has been seen to more than triple in M-band (4.67 μm; up to ∼150 GW/μm/sr) in just 1 month (i.e., two observations separated by 1 month), before decreasing again a month later (down to 30–40 GW/μm/sr) (de Pater et al., 2014). Other signs of energetic volcanic activity are the surface changes detected during and after the Galileo mission (P. Geissler et al., 2004; Davies et al., 2012).

In contrast, Loki Patera shows a quasi-periodic behavior, where the intensity increases every 440–540 days (de Kleer & de Pater, 2017; Rathbun & Spencer, 2006). The increase and subsequent decrease typically happen over a period of order 1–2 months each, separated by a ∼3-month period of high intensity (∼120 GW/μm/sr at 3.78 μm) (de Kleer & de Pater, 2017; de Pater et al., 2017; Howell et al., 2001). The most up-to-date Loki Patera graph of intensity versus time (de Kleer & Rathbun, 2023) shows that the volcano's last brightening event stretched over April–September 2021. Based on the 440–540 day period, the next brightening event would have been expected to start in August–October 2022. The Keck observations from August and September 2022 show that it was not particularly active. The JWST observations from mid-November 2022 revealed a much higher intensity. Based upon the quasi-periodic behavior of Loki Patera's brightening events, it is quite likely that JWST detected Loki Patera's most recent brightening event. Since it is close to the limb, it is difficult to determine a precise value for Loki Patera's intensity, but if we take the data at face value and correct for the emission angle effect (factor of 2.6), its spectrum would be close to that of Kanehekili Fluctus. We should keep in mind for both volcanoes, though, that JWST/NIRSpec's spatial sampling is quite low (0.1″/pixel), and hence neighboring volcanoes (e.g., Figure 5, but new eruptions may have appeared and old ones faded by November 2022) could have affected the measured intensity. However, since volcanoes are known to "repel" each other based upon the spatial distribution of hot spots and paterae (Hamilton et al., 2013), it may be unlikely that there are other hot spots adjacent to Loki Patera and Kanehekili Fluctus.

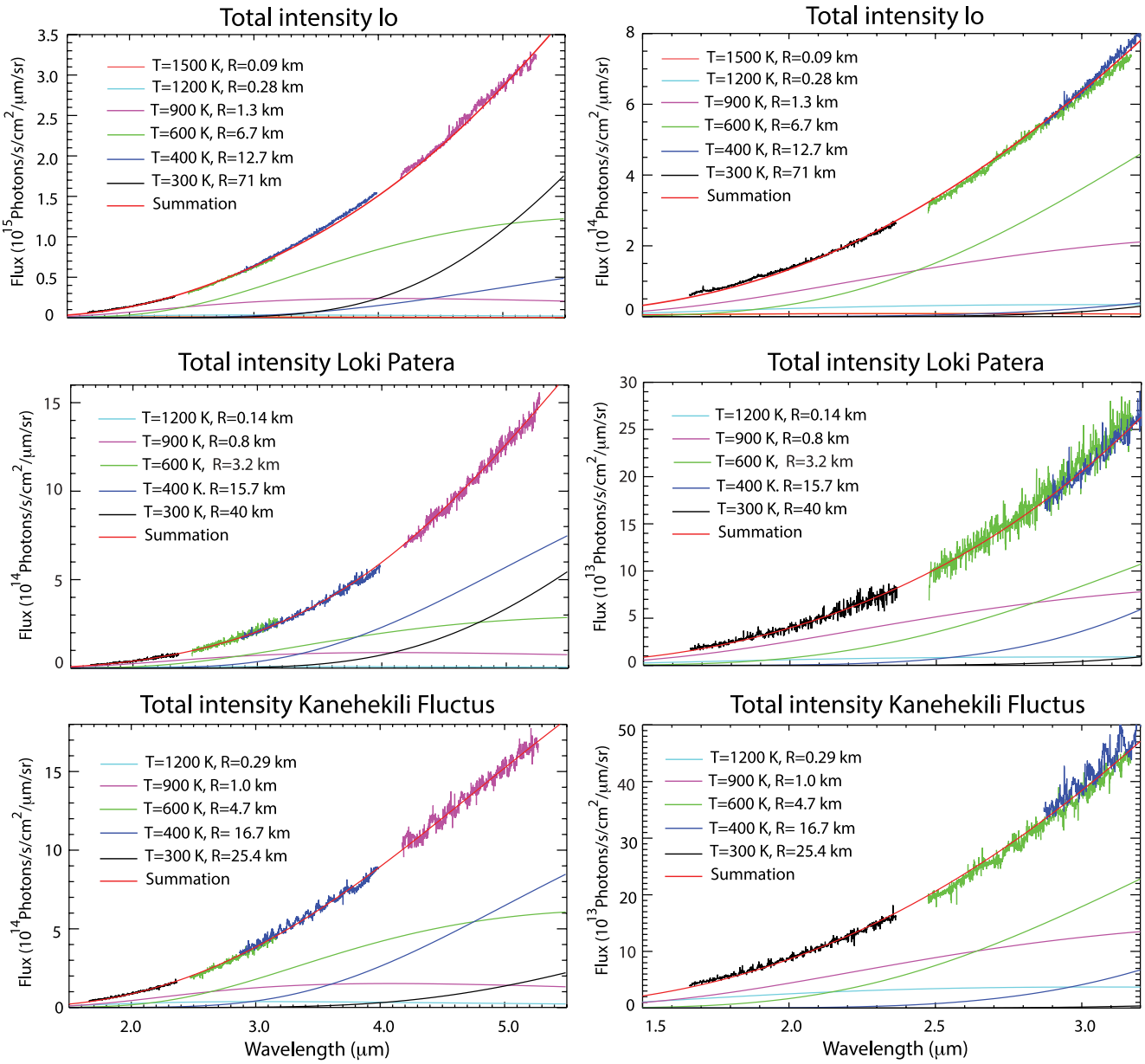

Figure 6. Spectra of the total intensity of Io, Loki Patera and Kanehekili Fluctus. The different colors of the data refer to the four different spectral regions of the G235H and G395H gratings. The data for Kanehekili Fluctus and Loki Patera were corrected for the emission angle effect (factors of 1.10 for Kanehekili Fluctus, and 2.5–2.8 for Loki Patera—2.5 for G395H, and 2.8 for G235H). Superposed are blackbody spectra at different temperatures, together with the relevant areas (indicated by a radius, assuming a circular area) as indicated. The red line shows the summation of these curves. On the left the entire observed spectra are shown (1.5–5.5 μm); on the right we show an enlargement of the 1.5–3.2 μm region.

Spectra in units of photons/s/cm^2/μm are shown in Figure 6. The spectra for Kanehekili Fluctus and Loki Patera in these plots were corrected for the emission angle effect. Superposed are blackbody curves for temperatures between 300 and 1,500 K, with different areas, as indicated. The sum of these curves match the observed spectra quite well, and show, as expected, that the spectra are consistent with cooling lava flows, with the hottest lavas covering the smallest areas. Blackbody curves that match the total intensity of Io show that the region covered by lavas with temperatures at/over 300 K cover an area of at least 15,000 km^2, and the temperature required to provide a good fit to the observed spectrum at the shortest wavelengths is ~1,200–1,500 K over a region of ~0.4 km^2. A 1,200–1,500 K temperature is consistent with a basaltic composition, which has a melting temperature of 1475 K. This is the most common lava composition on

21699100, 2023, 8, Downloaded from https://agupubs.onlinelibrary.wiley.com/doi/10.1029/2023JE007872 by Technical University Delft, Wiley Online Library on [15/08/2023]. See the Terms and Conditions (https://onlinelibrary.wiley.com/terms-and-conditions) on Wiley Online Library for rules of use; OA articles are governed by the applicable Creative Commons License

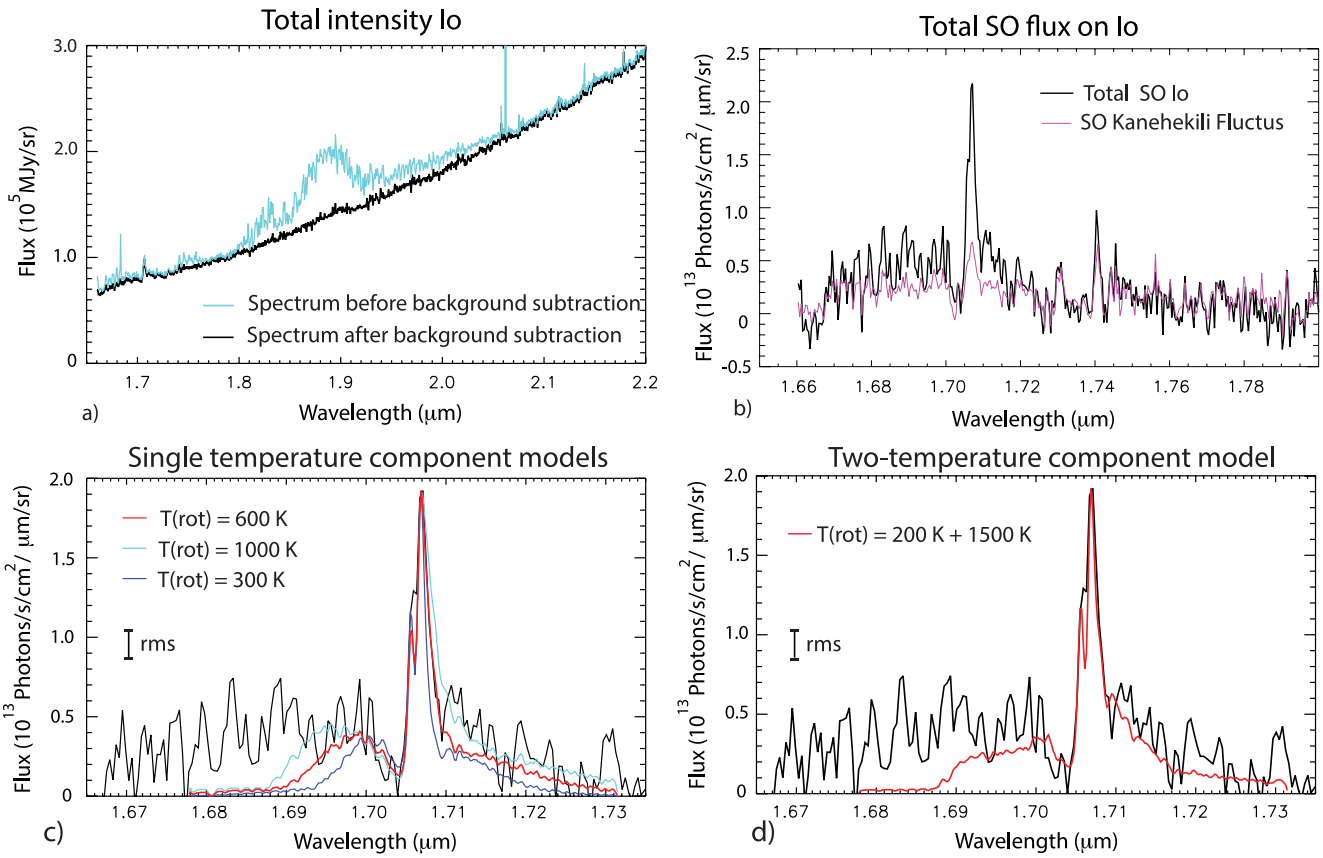

Figure 7. (a) Integrated intensity from Io, with the SO emission band at ∼1.707 μm. The black curve shows the spectrum after the background was subtracted, and bad pixels removed. The cyan curve shows the spectrum before background subtraction. (b) SO emission band after subtraction of the continuum emission. The black line shows the SO emission integrated over the entire disk; the pink line shows the emission over Kanehekili Fluctus, centered at the brightest pixel and integrated over a circle with a radius of 2.5 pixels (0.25″). The peak at 1.74 μm has not been detected before (Bernath & Bittner, 2020; de Pater et al., 2002; Laver et al., 2007); based on this, and the fact that several spaxels at this wavelength at Kanehekili Fluctus were brighter than surrounding spaxels (resembling the cosmic ray hits we replaced at other spaxels, as described in Section 2.1), we think this is an artifact. Since these spaxels are right at Kanehekili Fluctus, we did not want to change them. The 1-σ standard deviation (rms) as measured near 1.75–1.80 μm is indicated on the plot. (c) SO emission band integrated over the disk after subtraction of the continuum emission, as in panel (b). Superposed are models of the SO emission at a rotational temperature of 300 (blue curve), 600 (red curve), and 1,000 K (upper cyan curve). (d) SO emission band integrated over the disk with superposed de Kleer, de Pater, and Ádámkovics (2019)'s 2-temperature model, with a 200 and a 1,500 K component.

Earth, its Moon, and other terrestrial planets (Davies, 2007). Shorter wavelength spectra (such as the planned G140H/F100LP spectra with JWST NIRSpec) are needed to determine whether even higher eruption temperatures are present.

The highest measured temperature at the two volcanoes is ∼1,200 K, over an area of ∼0.25 km^2 at Kanehekili Fluctus and 0.06 km^2 at Loki Patera. These areal values for such a high temperature compare well with the previously derived numbers of ∼0.03–0.3 km^2 at individual volcanoes (Davies, 2003). Fits of a model of an overturning magma sea (de Kleer & de Pater, 2017; Matson et al., 2006) to the 1999 data of Loki Patera revealed a 1,100 K component over a 4 km^2 area (de Pater et al., 2017), which is close to the area covered by the combined 1,200 & 900 K blackbody curves. The blackbody fits in Figure 6 show that temperatures down to ∼300 K are needed to match the spectra, covering ∼2,000 km^2 at Kanehekili Fluctus and ∼5,000 km^2 at Loki Patera.

We note that although we did not conduct formal blackbody fits to the spectra (really, the temperature of a cooling lava flow should be a continuum from the eruption temperature down to the background equilibrium value), formal fits using the indicated temperatures would not differ that much from our values, since each blackbody curve provides a unique shape, and the sum of these shapes, each multiplied by the area that represents that temperature, constitutes the observed thermal emission spectrum. Also, a physical constraint on the model is that the regions of decreasing temperature should have increasing area. Assuming this simplified discretization of temperatures, the areas may be varied by perhaps 10% to still provide an acceptable fit.

21699100, 2023, 8, Downloaded from https://agupubs.onlinelibrary.wiley.com/doi/10.1029/2023JE007872 by Technical University Delft, Wiley Online Library on [15/08/2023]. See the Terms and Conditions (https://onlinelibrary.wiley.com/terms-and-conditions) on Wiley Online Library for rules of use; OA articles are governed by the applicable Creative Commons License

21699100, 2023, 8, Downloaded from https://agupubs.onlinelibrary.wiley.com/doi/10.1029/2023JE007872 by Technical University Delft, Wiley Online Library on [15/08/2023]. See the Terms and Conditions (https://onlinelibrary.wiley.com/terms-and-conditions) on Wiley Online Library for rules of use; OA articles are governed by the applicable Creative Commons License

4.2. SO Emissions

An image of just the SO emission, integrated over the center of the emission band (1.705–1.709 μm) is shown in Figure 2d. Emission is seen over much of the southern hemisphere, and in particular over Kanehekili Fluctus. A reprojection of the SO image superposed on a USGS map is shown in Figure 3b. The detailed distribution is clearly different from the spatial distribution in the continuum emission in panel (a), which provides some assurance that the continuum emission was properly subtracted. Both maps show a strong peak at Kanehekili Fluctus. While plumes above this volcano have been detected by the *Galileo* spacecraft (P. E. Geissler & McMillan, 2008), the gases in the plumes were not identified. The Kanehekili plumes were classified as Prometheus-type plumes, where the dust reached altitudes of order 100 km, and the gas about 400 km (P. E. Geissler & McMillan, 2008).

This is the first time we see such a strong spatial correlation between an active volcano (i.e., a hot spot) and 1.707-μm SO emission. While SO_2, SO, S_2 and S gases have been detected in plumes before (Jessup et al., 2007; McGrath et al., 2000; Pearl et al., 1979; Spencer et al., 2000), it is the first time the forbidden 1.707-μm emission from SO has been directly identified above a seemingly active volcano. As discussed by de Pater et al. (2002), since the emission is forbidden, and production of SO in the excited $a^1\Delta$ state in the atmosphere is highly improbable, the molecules are most likely excited thermodynamically at high temperatures (∼1500 K) before ejection from the vent. Since they radiate only once after exiting the collisional environment in the vent, one can estimate the SO venting rate from the observed emission rate. The maximum intensity of our SO emission profile is very similar to that observed in 1999 (∼5 photons/s/cm^2/μm when scaled to the observer–Io distance of 4.08 AU in 1999); therefore, the emission rate of SO from the vent is likely to be similar as well, that is, $\sim 2 \times 10^{27}$ excited SO molecules/s integrated over the disk, or ∼0.02% of the emission rate of $\sim 10^{31}$ SO_2 molecules/s as derived by Strobel and Wolven (2001). We note that de Pater et al. (2002) adopted a SO/SO_2 ratio of 0.10 to derive the quenching temperature of ∼1,500 K.

Panels (c) and (d) in Figure 3 show the spatial distribution of the SO emission integrated over the center of the emission band (1.705–1.709 μm), as observed in July 2010 and December 2015 (de Pater et al., 2020). The distribution in those years was very different, and the authors at that time concluded that there was no obvious correlation with hot spots. They attributed the emission to a large number of stealth plumes, produced when silicate melts interact with superheated SO_2 vapor at depth; the presence of such plumes was first suggested by Johnson et al. (1995) to explain the patchiness in the SO_2 atmosphere as inferred from UV and microwave observations. Although in 2010 and 2015 some hot spots did line up with SO emissions, there was no clear correlation. Our new observations show a clear correlation with the hot spot detected at Kanehekili Fluctus; this is the first time we observe the 1.707-μm SO emission from an active volcano that is known to be associated with plumes in the past. Hence, such volcanoes do seem to eject SO in the excited $a^1\Delta$ state, as hypothesized by de Pater et al. (2002). In addition, there also is a widespread component at roughly 30% of the peak flux, which is at a level similar to that observed in 2010 and 2015. This component is likely associated with stealth volcanism. It seems quite unlikely that it could have originated at Kanehekili Fluctus, and been spread out by winds before de-excitation. Since the Einstein A coefficient is 2.2 s^{-1} (Klotz et al., 1984), that is, the SO molecules will not stay in the excited state for more than a few seconds, not long enough to be spread out substantially by winds.

In Figures 7c and 7d we show the disk-integrated spectra with superposed models of the SO emission band, where the models were constructed assuming local thermodynamic equilibrium as in past work (de Kleer, de Pater, & Ádámkovics, 2019; de Pater et al., 2002, 2020). Panel (c) shows models for one rotational temperature; a temperature of 600 K (red line) matches the core of the line quite well. The width of the core of the emission band increases with the rotational temperature, as shown by the models for a 300 and 1,000 K temperature. The wings of the emission band are not well matched by any of these models, though. Panel (d) shows a comparison with de Kleer, de Pater, and Ádámkovics (2019)'s model that matched a disk-integrated spectrum with a much higher spectral resolution. This model consists of two temperatures: a low ∼200 K and a high ∼1,500 K, which were combined using $c_1F(T_1) + c_2F(T_2)$, with F the model intensity at temperature $T_1 \approx 200$ K and $T_2 = 1{,}500$ K, with $c_2/c_1 = 5/6$. As shown, this model matches the core of the emission band as well as the long-wavelength wing quite well, but falls short at 1.68–1.70 μm, just as seen in previous observations (de Pater et al., 2020). In fact, this part of the spectrum has always defied model fits; we do not know the cause of these mismatches. They may be caused by non-LTE effects, but to date no-one has managed to match the spectrum despite different approaches (Bernath & Bittner, 2020; de Pater et al., 2020). Perhaps there are as-of-yet unknown SO transitions, or an as-of-yet unidentified molecule.

4.3. SO Emissions and Lyman-α Radiation

In addition to the sources of SO forbidden ($a^1\Delta \rightarrow X^3\Sigma^-$) 1.707 μm emissions on Io discussed by de Pater et al. (2002), SO_2 dissociation by Ly-α is also a potential source of SO emission on Io. As shown in the following, however, this source does not appear to be strong enough to be a major contributor to the observed SO emission.

SO_2 is isoelectronic with O_3 and the latter preferentially dissociates at large photon energies in the Hartley bands into $O_2(a^1\Delta_g) + O(^1D)$ (Xie et al., 2017). For SO_2 there are two dissociation paths, one identical to O_3 for the SO + O channel and another for the O_2 + S channel (Miliordos & Xantheas, 2014). The strong UV absorption band of SO_2 in the 240–180 nm region is due to the dipole allowed $\left(\tilde{C}^1B_2 \leftarrow \tilde{X}^1A_1\right)$ transition and the $\tilde{C}^1B_2$ state correlates diabatically to $SO\left(\tilde{a}^1\Delta\right) + O(^1D)$, but in this wavelength range only the ground state products are energetically accessible, $SO(X^3\Sigma^-) + O(^3P)$.

The dissociation energy of SO_2 is 5.66 eV. The $SO\left(\tilde{a}^1\Delta\right)$ state is 0.726 eV above the ground state $SO(X^3\Sigma^-)$ and $O(^1D)$ is 1.968 eV above $O(^3P)$. Thus, dissociation to produce singlet products: $SO_2\left(\tilde{X}^1A_1\right) + h\nu(100.5 < \lambda < 148.4\ nm) \rightarrow SO\left(\tilde{a}^1\Delta\right) + O(^1D)$, requires 8.34 eV and is probably terminated at 12.349 eV, the ionization threshold of SO_2. In this wavelength range, the solar spectrum is dominated by the strong solar Lyman-α line at 121.6 nm. A representative value for the solar Lyman-α flux at 1 AU is 4×10^{11} photons/s/cm^2 (equivalent to 0.0065 W/m^2/nm, based on measurements by the TIMED satellite). At 5 AU, the solar Lyman-α flux is 1.6×10^{10} photons/s/cm^2. When Io is in Jupiter's shadow, there is still Lyman-α radiation from solar Lyman-α radiation scattered by H atoms in the interplanetary medium (IPM). At Jupiter, this IPM Lyman-α is approximately $4\pi I_{IPM} = 700$ R (Melin & Stallard, 2016). Assuming that this component is isotropic, then $I_{IPM} = 5.5 \times 10^7$ photons/s/cm^2/sr. For these photons in a purely absorbing plane-parallel SO_2 atmosphere, the equation of radiative transfer is $\mu dI/d\tau = I$. The quantity $\mu = \cos$ (zenith angle), which is positive in the upward direction, and the zenith angle = 0 in the radially outward direction. The optical depth $d\tau = -\sigma Ly\alpha_{SO_2} n(SO_2) dz$ with $\sigma Ly\alpha_{SO_2}$ the SO_2 photoabsorption (photodissociation) cross section at Lyman-α.

The solution to the equation $\mu dI/d\tau = I$ is:

$$I(\tau, \mu) = I_{IPM} \exp(\tau/\mu), \tag{3}$$

and the downward directed flux into the atmosphere is

$$F_d(\tau) = \int_{-1}^{0} I(\tau, \mu)\mu d\mu. \tag{4}$$

The excitation rate per SO_2 molecule is:

$$J_{SO_2}(\tau) = \sigma Ly\alpha_{SO_2} n_{SO_2}(\tau) I_{IPM} \int_{-1}^{0} \exp\left(\frac{\tau}{\mu}\right) d\mu, \tag{5}$$

with $\sigma Ly\alpha SO_2 = 3.8 \times 10^{-17}$ cm^2 and the total column excitation rate is:

$$Jtot_{SO_2}(\tau) = \sigma Ly\alpha_{SO_2} \int_0^{\tau} n_{SO_2}(\tau) \left[I_{IPM} \int_{-1}^{0} \exp\left(\frac{\tau}{\mu}\right) d\mu \right] d\tau, \tag{6}$$

In the limit of large optical depth, $Jtot_{SO_2}(\tau \rightarrow \infty) = 0.5 I_{IPM} = 2.3 \times 10^7$/s/cm^2, and if the SO_2 were optically thick ($\gtrsim 5 \times 10^{16}$ SO_2 molecules/cm^2) over the entire disk of Io $\left(\pi R_{Io}^2\right)$, this would yield ~$2.5 \times 10^{24}$ photons/s. However, when Io is in direct sunlight, then $Jtot_{SO_2}$ at large optical depths is 1.6×10^{10}/s/cm^2 and integrated over the entire disk of $\left(\pi R_{Io}^2\right)$, this would yield ~$2 \times 10^{27}$ photons/s. If all SO_2 dissociation by Lyman-α yields one 1.707-μm photon, then our JWST observations of the 1.707-μm SO transition could be explained by this mechanism if Io were in direct sunlight, but not when Io is in Jupiter's shadow.

On the Jovian nightside atmosphere there is a hydrogen Lyman-α "bulge" with brightness of up to 1.5 kR (Melin & Stallard, 2016), which is equal to or greater than the IPM intensity, which can be compared with the dayside Lyman-α "bulge" of 22 kR. The mechanisms that produce these brightness bulges are not entirely understood, but Jupiter's upper atmosphere has a large scattering optical depth that scatters incoming Lyman-α photons back to space with very few undergoing absorptions in the lower atmosphere. If the nightside bulge were not due to IPM Lyman-α, then it is potentially an additional source to dissociate SO_2 and yield SO 1.707-μm photons. The

21699100, 2023, 8, Downloaded from https://agupubs.onlinelibrary.wiley.com/doi/10.1029/2023JE007872 by Technical University Delft, Wiley Online Library on [15/08/2023]. See the Terms and Conditions (https://onlinelibrary.wiley.com/terms-and-conditions) on Wiley Online Library for rules of use; OA articles are governed by the applicable Creative Commons License

21699100, 2023, 8, Downloaded from https://agupubs.onlinelibrary.wiley.com/doi/10.1029/2023JE007872 by Technical University Delft, Wiley Online Library on [15/08/2023]. See the Terms and Conditions (https://onlinelibrary.wiley.com/terms-and-conditions) on Wiley Online Library for rules of use; OA articles are governed by the applicable Creative Commons License

authors are not aware of any Jupiter calculations of resonance scattering of solar Lyman-α photons from the subsolar point to the anti-solar point, but for the Earth's Lyman-α geocorona the ratio is ~35:1 kR with ~14 kR at the terminator (Strobel et al., 1974). Depending on the location of Io in Jupiter's shadow, resonance scattering could be an additional source, but not the entire source of SO 1.707-μm photons.

5. Conclusions

Io was observed with JWST's NIRSpec/IFU with the G235H/F170LP and G395H/F290LP settings on 15 November 2022, at a resolving power $R \approx 2{,}700$. Kanehekili Fluctus was exceptionally bright, and Loki Patera had just entered a new brightening phase. We detected the 1.707 μm forbidden SO emission band complex at the location of Kanehekili Fluctus. This is the first time that this emission has been seen above an active volcano, and suggests that the origin of such emissions is indeed ejection directly from the vent in an excited state. Low emission levels were also seen over large fractions of Io's surface, in particular at latitudes between 0° and 40°S. In the present paper we rule out potential excitation by the Lyman-α flux from the interplanetary medium, hence strengthening conclusions from 2010 to 2,015 observations that the SO 1.707 μm emissions may originate from stealth volcanism (de Pater et al., 2020).

In addition to these emissions, the 1.65–5.3 μm continuum spectra of Kanehekili Fluctus and Loki Patera, the two brightest volcanoes during the observations, are consistent with eruptions from a small venting area (either a volcanic vent, or opening in an overturning lava lake), cooling and spreading over time. After correction for the emission angle, the maximum temperature resolved in our observations for both Kanehekili Fluctus and Loki Patera was ~1200 K over an area ~0.25 km^2 for Kanehekili Fluctus and 0.06 km^2 for Loki Patera. Lower temperatures covered progressively larger areas, up to almost 2,000 km^2 at 300 K for Kanehekili Fluctus and ~5,000 km^2 for Loki Patera.

Additional observations of the 1.707 μm forbidden SO emissions are scheduled to be obtained with JWST in August 2023.

Data Availability Statement

The data were obtained from the Mikulski Archive for Space Telescopes at the Space Telescope Science Institute, Observation #24 of ERS program #1373. The specific observations analyzed can be accessed with de Pater (2023) [Data set]. The data were reduced with the standard JWST pipeline, as described in Section 2.1 (JWST pipeline, n.d. [Software]). The resulting fits files were read into IDL, and aligned by using the Fast Fourier transform (FFT) cross-correlation algorithm in IDL. To make spectra the authors used IDL routine apphot.pro (Perrin, 2013 [Software]), after expanding the images by a factor of 5, and interpolating to the smaller-sized pixels.

Acknowledgments
This work is based on observations made with the NASA/ESA/CSA James Webb Space Telescope. The data were obtained from the Mikulski Archive for Space Telescopes at the Space Telescope Science Institute, which is operated by the Association of Universities for Research in Astronomy, Inc., under NASA contract NAS 5-03127 for JWST. These observations are associated with program #1373 (Observation #24), which is led by co-PIs Imke de Pater and Thierry Fouchet and has a zero-exclusive-access period. We thank Julie Rathbun for providing the digital data for Loki Patera's quasi-periodic behavior in 2020–2022, as well as John Spencer and Jani Radebaugh for constructive comments on the paper. IdP, MHW, EMM, CM, PMF, MS, MST are in part supported by the Space Telescope Science Institute grant nr. JWST-ERS-01373. TF and EL acknowledge support from ANR Grant ANR-21-CE49-0020-01. LNF was supported by a European Research Council Consolidator Grant (under the European Union's Horizon 2020 research and innovation programme, grant agreement No 723890) at the University of Leicester. RH was supported by Grant PID2019-109467GB-I00 through MCIN/AEI/10.13039/501100011033/and by Grupos Gobierno Vasco IT1742-22. KdK acknowledges support from NASA through Grant HST-GO-15425.002-A from the Space Telescope Science Institute, which is operated by AURA, Inc., under NASA contract NAS 5-26555. Some of this research was carried out at the Jet Propulsion Laboratory, California Institute of Technology, under a contract with the National Aeronautics and Space Administration (80NM0018D0004).

References

Bernath, P. F., & Bittner, D. M. (2020). Line list for the $a^1\Delta$-$X^3\Sigma^-$ transition of SO: Assignment of the 1.69 micron feature on Io. *Journal of Quantitative Spectroscopy and Radiative Transfer*, *240*, 106686. https://doi.org/10.1016/j.jqsrt.2019.106686

Bohlin, R. C., & Landolt, A. U. (2015). The CALSPEC stars P177D and P330E. *The Astronomical Journal*, *149*(4), 122. https://doi.org/10.1088/0004-6256/149/4/122

Cantrall, C., de Kleer, K., de Pater, I., Williams, D. A., Davies, A. G., & Nelson, D. (2018). Variability and geologic associations of volcanic activity on Io in 2001–2016. *Icarus*, *312*, 267–294. https://doi.org/10.1016/j.icarus.2018.04.007

Davies, A. G. (2003). Volcanism on Io: Estimation of eruption parameters from Galileo NIMS data. *Journal of Geophysical Research*, *108*(E9), 5106. https://doi.org/10.1029/2001JE001509

Davies, A. G. (2007). *Volcanism on Io: A comparison with Earth* (p. 372). Cambridge University Press. https://doi.org/10.1017/CBO9781107279902

Davies, A. G. (2022). Cautionary analysis of spectral radiance from Io's active volcanoes derived from galileo near-infrared mapping spectrometer data. *The Astronomical Journal*, *163*(1), 2. https://doi.org/10.3847/1538-3881/ac3012

Davies, A. G., Veeder, G. J., Matson, D. L., & Johnson, T. V. (2012). Charting thermal emission variability at Pele, Janus Patera and Kanehekili Fluctus with the *Galileo* NIMS Io Thermal Emission Database (NITED). *Icarus*, *221*(1), 466–470. https://doi.org/10.1016/j.icarus.2012.04.012

de Kleer, K., & de Pater, I. (2016). Time variability of Io's volcanic activity from near-IR adaptive optics observations on 100 nights in 2013–2015. *Icarus*, *280*, 378–404. https://doi.org/10.1016/j.icarus.2016.06.019

de Kleer, K., & de Pater, I. (2017). Io's Loki Patera: Modeling of three brightening events in 2013–2016. *Icarus*, *289*, 181–198. https://doi.org/10.1016/j.icarus.2017.01.038

de Kleer, K., de Pater, I., & Ádámkovics, M. (2019a). Emission from volcanic SO gas on Io at high spectral resolution. *Icarus*, *317*, 104–120. https://doi.org/10.1016/j.icarus.2018.07.012

de Kleer, K., de Pater, I., Molter, E. M., Banks, E., Davies, A. G., Alvarez, C., et al. (2019b). Io's volcanic activity from time domain adaptive optics observations: 2013-2018. *The Astronomical Journal*, *158*(1), 29. https://doi.org/10.3847/1538-3881/ab2380

de Kleer, K., & Rathbun, J. (2023). Io's thermal emission and heat flow. In R. L. Lopes, K. de Kleer, & J. T. Keane (Eds.), *Io: A new view of Jupiter's Moon*, *Astrophysics and Space Science Library* (Vol. 468). Springer.

de Pater, I. (2023). STSci/MAST [Dataset]. Data from ERS Io eclipse program 1373. https://doi.org/10.17909/aprz-gg78

de Pater, I., Davies, A. G., McGregor, A., Trujillo, C., Ádámkovics, M., Veeder, G. J., et al. (2014). Global near-IR maps from Gemini-N and Keck in 2010, with a special focus on Janus Patera and Kanehekili Fluctus. *Icarus*, *242*, 379–395. https://doi.org/10.1016/j.icarus.2014.06.019

de Pater, I., de Kleer, K., & Ádámkovics, M. (2020). High spatial and spectral resolution observations of the forbidden 1.707 μm rovibronic SO emissions on Io: Evidence for widespread stealth volcanism. *The Planetary Science Journal*, *1*(2), 29. https://doi.org/10.3847/PSJ/ab9eb1

de Pater, I., de Kleer, K., Davies, A. G., & Ádámkovics, M. (2017). Three decades of Loki Patera observations. *Icarus*, *297*, 265–281. https://doi.org/10.1016/j.icarus.2017.03.016

de Pater, I., Fouchet, T., Wong, M., Fry, P., Fletcher, L., Hueso, R., et al. (2022). JWST observations of the Jovian system from commissioning and ERS data. *AAS/Division for Planetary Sciences Meeting Abstracts*, *54*, 306–307.

de Pater, I., Laver, C., Marchis, F., Roe, H. G., & Macintosh, B. A. (2007). Spatially resolved observations of the forbidden SO a1Δ → X3Σ− rovibronic transition on Io during an eclipse and a volcanic eruption at Ra Patera. *Icarus*, *191*(1), 172–182. https://doi.org/10.1016/j.icarus.2007.04.011

de Pater, I., Marchis, F., Macintosh, B. A., Roe, H. G., Le Mignant, D., Graham, J. R., & Davies, A. G. (2004). Keck AO observations of Io in and out of eclipse. *Icarus*, *169*(1), 250–263. https://doi.org/10.1016/j.icarus.2003.08.025

de Pater, I., Roe, H., Graham, J. R., Strobel, D. F., & Bernath, P. (2002). Note: Detection of the forbidden SO $a^1\Delta \rightarrow X^3\Sigma^-$ rovibronic transition on Io at 1.7 μm. *Icarus*, *156*(1), 296–301. https://doi.org/10.1006/icar.2001.6787

Geissler, P., McEwen, A., Phillips, C., Keszthelyi, L., & Spencer, J. (2004). Surface changes on Io during the Galileo mission. *Icarus*, *169*(1), 29–64. https://doi.org/10.1016/j.icarus.2003.09.024

Geissler, P. E., & McMillan, M. T. (2008). Galileo observations of volcanic plumes on Io. *Icarus*, *197*(2), 505–518. https://doi.org/10.1016/j.icarus.2008.05.005

Hamilton, C. W., Beggan, C. D., Still, S., Beuthe, M., Lopes, R. M. C., Williams, D. A., et al. (2013). Spatial distribution of volcanoes on Io: Implications for tidal heating and magma ascent. *Earth and Planetary Science Letters*, *361*, 272–286. https://doi.org/10.1016/j.epsl.2012.10.032

Howell, R. R., Spencer, J. R., Goguen, J. D., Marchis, F., Prangé, R., Fusco, T., et al. (2001). Ground-based observations of volcanism on Io in 1999 and early 2000. *Journal of Geophysical Research*, *106*(E12), 33129–33140. https://doi.org/10.1029/2000JE001382

Jessup, K. L., Spencer, J., & Yelle, R. (2007). Sulfur volcanism on Io. *Icarus*, *192*(1), 24–40. https://doi.org/10.1016/j.icarus.2007.06.025

Johnson, T. V., Matson, D. L., Blaney, D. L., Veeder, G. J., & Davies, A. (1995). Stealth plumes on Io. *Geophysical Research Letters*, *22*(23), 3293–3296. https://doi.org/10.1029/95GL03084

JWST pipelines. (n.d.). Retrieved from https://jwst-docs.stsci.edu/jwst-science-calibration-pipeline-overview

Klotz, R., Marian, C. M., Peyerimhoff, S. D., Hess, B. A., & Buenker, R. J. (1984). Calculation of spin-forbidden radiative transitions using correlated wavefunctions: Lifetimes of $b^1\Sigma^+$, $a^1\Delta$ states in O_2, S_2 and SO. *Chemical Physics*, *89*(2), 223–236. https://doi.org/10.1016/0301-0104(84)85311-2

Laver, C., de Pater, I., Roe, H., & Strobel, D. F. (2007). Temporal behavior of the SO 1.707 μm ro-vibronic emission band in Io's atmosphere. *Icarus*, *189*(2), 401–408. https://doi.org/10.1016/j.icarus.2007.02.008

Matson, D. L., Davies, A. G., Veeder, G. J., Rathbun, J. A., Johnson, T. V., & Castillo, J. C. (2006). Io: Loki Patera as a magma sea. *Journal of Geophysical Research*, *111*(E9), E09002. https://doi.org/10.1029/2006JE002703

McGrath, M. A., Belton, M. J. S., Spencer, J. R., & Sartoretti, P. (2000). Spatially resolved spectroscopy of Io's Pele plume and SO_2 atmosphere. *Icarus*, *146*(2), 476–493. https://doi.org/10.1006/icar.1999.6412

Melin, H., & Stallard, T. S. (2016). Jupiter's hydrogen bulge: A Cassini perspective. *Icarus*, *278*, 238–247. https://doi.org/10.1016/j.icarus.2016.06.023

Miliordos, E., & Xantheas, S. S. (2014). On the bonding nature of ozone (O_3) and its sulfur-substituted analogues SO_2, OS_2, and S_3: Correlation between their biradical character and molecular properties. *Journal of the American Chemical Society*, *136*(7), 2808–2817. https://doi.org/10.1021/ja410726u

Mura, A., Adriani, A., Tosi, F., Lopes, R. M. C., Sindoni, G., Filacchione, G., et al. (2020). Infrared observations of Io from Juno. *Icarus*, *341*, 113607. https://doi.org/10.1016/j.icarus.2019.113607

Peale, S. J., Cassen, P., & Reynolds, R. T. (1979). Melting of Io by tidal dissipation. *Science*, *203*(4383), 892–894. https://doi.org/10.1126/science.203.4383.892

Pearl, J., Hanel, R., Kunde, V., Maguire, W., Fox, K., Gupta, S., et al. (1979). Identification of gaseous SO_2 and new upper limits for other gases on Io. *Nature*, *280*(5725), 755–758. https://doi.org/10.1038/280755a0

Perrin, S. M. (2013). Retrieved from https://www.stsci.edu/~mperrin/software/sources/

Rathbun, J. A., & Spencer, J. R. (2006). Loki, Io: New ground-based observations and a model describing the change from periodic overturn. *Geophysical Research Letters*, *33*(17), L17201. https://doi.org/10.1029/2006GL026844

Rayner, J. T., Cushing, M. C., & Vacca, W. D. (2009). The infrared telescope facility (IRTF) spectral library: Cool stars. *The Astrophysical Journal Supplement*, *185*(2), 289–432. https://doi.org/10.1088/0067-0049/185/2/289

Spencer, J. R., Jessup, K. L., McGrath, M. A., Ballester, G. E., & Yelle, R. (2000). Discovery of Gaseous S_2 in Io's Pele plume. *Science*, *288*(5469), 1208–1210. https://doi.org/10.1126/science.288.5469.1208

Strobel, D. F., & Wolven, B. C. (2001). The atmosphere of Io: Abundances and sources of sulfur dioxide and atomic hydrogen. *Astrophysics and Space Science*, *277*, 271–287. https://doi.org/10.1023/A:1012261209678

Strobel, D. F., Young, T. R., Meier, R. R., Coffey, T. P., & Ali, A. W. (1974). The nighttime ionosphere: E region and lower F region. *Journal of Geophysical Research*, *79*(22), 3171–3178. https://doi.org/10.1029/JA079i022p03171

Trumbo, S. K., Brown, M. E., Bockelée-Morvan, D., de Pater, I., & Fouchet, T. (2023). Hydrogen peroxide at the poles of Ganymede. *Science Advances*, *3*(12), 272.

Williams, D. A., Wilson, A. H., & Greeley, R. (2000). A komatiite analog to potential ultramafic materials on Io. *Journal of Geophysical Research*, *105*(E1), 1671–1684. https://doi.org/10.1029/1999JE001157

Xie, C., Jiang, B., Kłos, J., Kumar, P., Alexander, M. H., Poirier, B., & Guo, H. (2017). Final state resolved quantum predissociation dynamics of $SO_2(\tilde{C}^1B_2)$ and its isotopomers via a crossing with a singlet repulsive state. *Journal of Physical Chemistry A*, *121*(26), 4930–4938. https://doi.org/10.1021/acs.jpca.7b04629

21699100, 2023, 8, Downloaded from https://agupubs.onlinelibrary.wiley.com/doi/10.1029/2023JE007872 by Technical University Delft, Wiley Online Library on [15/08/2023]. See the Terms and Conditions (https://onlinelibrary.wiley.com/terms-and-conditions) on Wiley Online Library for rules of use; OA articles are governed by the applicable Creative Commons License